Predictable surface emission patterns in terahertz photonic-crystal quantum cascade lasers

Y. Chassagneux[1*], R. Colombelli[1*], W. Maineult[2], S. Barbieri[2], S. P. Khanna[3], E. H. Linfield[3], and A. G. Davies[3]

[1]*Institut d'Electronique Fondamentale, Université Paris-Sud and CNRS, UMR8622, 91405 Orsay, France*

[2]*Laboratoire MPQ, Université Paris 7 and CNRS, UMR7162, 75013 Paris, France*

[3]*School of Electronic and Electrical Engineering, University of Leeds, Leeds LS2 9JT, United Kingdom*

[*]*Corresponding authors: yannick.chassagneux@u-psud.fr, raffaele.colombelli@u-psud.fr*

Abstract: We demonstrate a framework to understand and predict the far-field emission in terahertz frequency photonic-crystal quantum cascade lasers. The devices, which employ a high-performance three-well active region, are lithographically tunable and emit in the 104-120 μm wavelength range. A peak output power of 7 mW in pulsed mode is obtained at 10 K, and the typical device maximum operating temperature is 136 K. We identify the photonic-crystal band-edge states involved in the lasing process as originating from the hexapole and monopole modes at the Γ point of the photonic band structure, as designed. The theoretical far-field patterns, obtained via finite-difference time-domain simulations, are in excellent agreement with experiment. Polarization measurements further support the theory, and the role of the bonding wires in the emission process is elucidated.

OCIS codes: (140.5960) Semiconductor lasers; (230.5750) Resonators; (240.6680) Surface plasmons

References and links

1. K. Sakay, *Terahertz optoelectronics* (New York: Springer, 2005).
2. D. Mittleman, *Sensing with Terahertz radiation* (New York: Springer Books, 2004).
3. R. Köhler, A. Tredicucci, F. Beltram, H. E. Beere, E. H. Linfield, A. G. Davies, D. A. Ritchie, R. C. Iotti, and F. Rossi, "THz semiconductor-heterostructure laser," Nature (London) **417**, 156 (2002).
4. B. S. Williams, "Terahertz quantum cascade lasers," Nat. Photon. **1**, 517–525 (2007).
5. C. Walther, M. Fischer, G. Scalari, R. Terazzi, N. Hoyler, and J. Faist, "Quantum cascade lasers operating from 1.2 to 1.6 THz," Appl. Phys. Lett. **91**, 131122 (2007).
6. M. A. Belkin, J. A. Fan, S. Hormoz, F. Capasso, S. Khanna, M. Lachab, A. G. Davies, and E. H. Linfield, "Terahertz quantum cascade lasers with copper metal-metal waveguides operating up to 178 K," Opt. Express **16**, 3242 (2008).
7. K. Unterrainer, R. Colombelli, C. Gmachl, F. Capasso, H. Y. Hwang, A. M. Sergent, D. L. Sivco, and A. Y. Cho, "Quantum cascade lasers with double metal-semiconductor waveguide resonators," Appl. Phys. Lett. **80**, 3060–3062 (2002).
8. S. Kohen, B. Williams, and Q. Hu, "Electromagnetic modeling of terahertz quantum cascade laser waveguides and resonators," J. Appl. Phys. **97**, 053106 (2005).
9. A. J. L. Adam, I. Kašalynas, J. N. Hovenier, T. O. Klaassen, J. R. Gao, E. E. Orlova, B. S. Williams, S. Kumar, Q. Hu, and J. L. Reno, "Beam patterns of terahertz quantum cascade lasers with subwavelength cavity dimensions," Appl. Phys. Lett. **88**, 151105 (2006).

#106640 - $15.00 USD Received 21 Jan 2009; revised 3 Apr 2009; accepted 5 Apr 2009; published 22 May 2009

10. M. I. Amanti, M. Fischer, C. Walther, G. Scalari, and J. Faist, "Horn antennas for terahertz quantum cascade lasers," Electron. Lett. **43**, 573 (2007).
11. Y. Chassagneux, R. Colombelli, W. Maineult, S. Barbieri, H. E. Beere, D. A. Ritchie, S. P. Khanna, E. H. Linfield, and G. A. Davies, "Electrically pumped photonic crystal terahertz lasers controlled by boundary conditions," Nature (London) **457**, 174 (2009).
12. H. Luo, S. R. Laframboise, Z. R. Wasilewski, G. C. Aers, H. C. Liu, and J. C. Cao, "Terahertz quantum-cascade lasers based on a three-well active module," Appl. Phys. Lett. **90**, 041112 (2007).
13. Y. Chassagneux, J. Palomo, R. Colombelli, S. Dhillon, C. Sirtori, H. E. Beere, J. Alton, and D. A. Ritchie, "Terahertz microcavity lasers with subwavelength mode volumes and thresholds in the milliampere range," Appl. Phys. Lett. **90**, 091113 (2007).
14. P. Gellie, W. Maineult, A. Andronico, G. Leo, C. Sirtori, S. Barbieri, Y. Chassagneux, J. R. Coudevylle, R. Colombelli, S. P. Khanna, E. H. Linfield, and A. G. Davies, "Effect of transverse mode structure on the far field pattern of metal-metal terahertz quantum cascade lasers," J. Appl. Phys. **104**, 124513 (2008).
15. M. Bahriz, V. Moreau, R. Colombelli, O. Crisafulli, and O. Painter, "Design of mid-IR and THz quantum cascade laser cavities with complete TM photonic bandgap," Opt. Express **15**, 5948 (2007).
16. B. Williams, S. Kumar, Q. Hu, and J. L. Reno, "Distributed-feedback terahertz quantum cascade lasers with laterally corrugated metal waveguides," Opt. Lett. **30**, 2909–2911 (2005).
17. G. A. Samara, "Temperature and pressure dependences of the dielectric constants of semiconductors," Phys. Rev. B **27**, 3494–3505 (1983).
18. J. Vučković, M. Loncar, H. Mabchi, and A. Scherer, "Optimization of the Q factor in photonic crystal microcavities," IEEE J. Quantum Electron. **38**, 850 (2002).
19. S. H. Kim, S. K. Kim, and Y. H. Lee, "Vertical beaming of a wavelength-scale photonic crystal resonator," Phys. Rev. B **73**, 235117 (2006).
20. A. Taflove and S. C. Hagness, *Computational Electrodynamics: The Finite-Difference Time-Domain Method* (Norwood, MA: Artech, 2000).
21. A. Farjadpour, D. Roundy, A. Rodriguez, M. Ibanescu, P. Bermel, J. D. Joannopoulos, S. G. Johnson, and G. Burr, "Improving accuracy by subpixel smoothing in FDTD," Opt. Lett. **31**, 2972–2974 (2006).
22. M. Imada, A. Chutinan, S. Noda, and M. Mochizuki, "Multidirectionally distributed feedback photonic crystal lasers," Phys. Rev. B **65**, 195306 (2002).

1. Introduction

Compact sources of terahertz (THz) frequency radiation - which is approximately defined as the region between 0.5 THz and 5 THz [1] - have potential applications in several areas of science and technology including astronomy, environmental monitoring and bio-security [2]. The demonstration in 2002 of quantum cascade (QC) lasers operating in this spectral region [3] was an important breakthrough, and the QC laser is now an emergent compact source for narrowband THz radiation [4, 5]. Currently, devices with the best temperature performance [6] employ metal-metal waveguides, where the optical mode is highly confined between two metal plates [7]. However, low output powers [8] and extremely non-uniform far-field emission patterns [9, 10] are major drawbacks of THz QC lasers fabricated with such waveguides.

We have recently demonstrated a class of THz semiconductor laser where a photonic-crystal (PC) structure is written in the top metallization layer [11]. This simple technology yields lithographically-tunable, single-mode operation and angularly narrow, but not always single-lobed, surface-emission from metal-metal waveguides. In this paper, we provide a framework for predictive far-field emission engineering for this class of devices. Our far-field simulations are in excellent agreement with the experimental results, and also explain the action of the wire bonding on the emission pattern. First, we demonstrate high-performance THz QC lasers emitting at 2.7 THz and operating up to 165 K. We then describe the fabrication of surface-emitting PC devices based on the same semiconductor material. A maximum operating temperature (T_{max}) of 136 K is obtained, with peak output powers of 7 mW at 10 K and $\geq$4 mW at 78 K. Finally, the far-field emission patterns and polarizations are measured and compared with the theoretical model.

#106640 - $15.00 USD Received 21 Jan 2009; revised 3 Apr 2009; accepted 5 Apr 2009; published 22 May 2009

2. Active region quantum design

The active region is based on the three-well resonant-phonon design reported in Ref. [12]. This design yielded the highest maximum operating temperature (178 K) for THz QC lasers at a frequency of 3.1 THz [6]. The conduction band profile of our structure is shown in Fig. 1. The frequency of the radiative transition (between levels 4 and 3) is 2.69 THz by design, corresponding to ≈ 90 cm^{-1}.

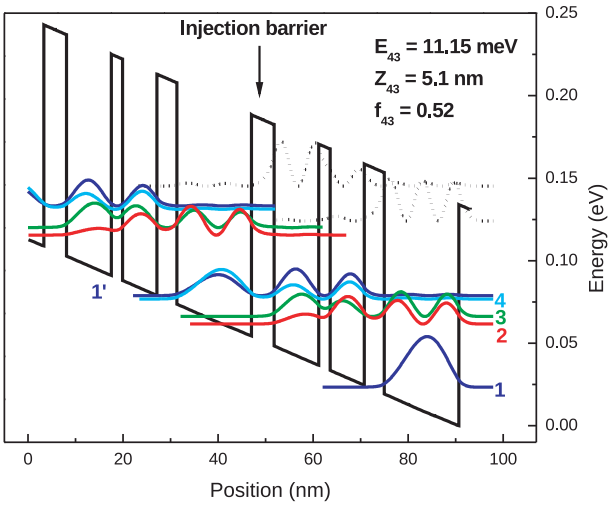

Fig. 1. Conduction band profile of two periods of the GaAs/$Al_{0.15}Ga_{0.85}As$ QC heterostructure. The moduli squared and energies of the wavefunctions are shown. The wavefunctions which are relevant to the laser operation are in color. The applied electric field is 12.5 kV/cm, i.e. 54.6 meV per period. The layer thicknesses - from left to right starting from the injection barrier - are **4.8**/9.4/**2.4**/7.2/**4.2**/15.7 nm (The AlGaAs barriers are in bold). The central 5.5 nm of the 15.7 nm-thick quantum well is n-doped with silicon to a level of 5.0x10^{16} cm^{-3}. The energy of the laser transition (E_{43}), its dipole matrix element (z_{43}) and the corresponding oscillator strength (f_{43}) are reported in the upper right corner of the figure.

The laser heterostructure (wafer L207) was grown by molecular beam epitaxy on an undoped GaAs substrate. After a 250-nm-thick undoped GaAs buffer layer, a 300-nm-thick $Al_{0.5}Ga_{0.5}As$ etch-stop layer was grown, followed by an 80-nm-thick layer of GaAs n-doped with silicon at 5x10^{18} cm^{-3}. The core consists of 226 stages of the active region of Fig. 1, giving a total thickness of $\approx$ 10 μm. The growth was concluded by a 50-nm-thick GaAs capping layer, n-doped at 5x10^{18} cm^{-3}. Following growth, the QC wafer was thermo-compressively bonded with gold onto an n-GaAs wafer following the procedure in Ref. [13], and the undoped substrate removed. Laser ridges 80, 140, 200, and 300 μm wide were then defined by contact optical lithography followed by wet chemical etching down to the lower, thermo-compressively bonded, metal layer. Ti/Au contacts (8/200 nm) were used as a top metallization. After backside polishing to give an n-GaAs substrate thickness of 200 μm, the devices were cleaved into laser bars (1.5 and 2 mm long), indium soldered to copper blocks, wire bonded, and mounted in a continuous flow liquid helium cryostat for device characterization.

Devices were tested in pulsed mode (typically at 0.3% duty cycle) at several heat-sink temperatures. Figure 2 presents typical results obtained. Figure 2(a) shows the light-current (L-I) and voltage-current (V-I) characteristics. The threshold current density (J_{th}) is 860 A/cm^2 at 10 K, and 910 A/cm^2 at 78 K. A typical laser spectrum is shown in the inset to Fig. 2(b) and ex-

#106640 - $15.00 USD Received 21 Jan 2009; revised 3 Apr 2009; accepted 5 Apr 2009; published 22 May 2009

tends over a broad range, from 2.25 THz to 2.73 THz, i.e. an interval of 480 GHz. Fig. 2(b) also shows the laser current threshold density as a function of heat-sink temperature. An excellent T_{max} of 165 K is obtained in pulsed mode, which is comparable to the figure achieved in Ref. [6] when using gold, rather than copper, as the metal for the waveguides.

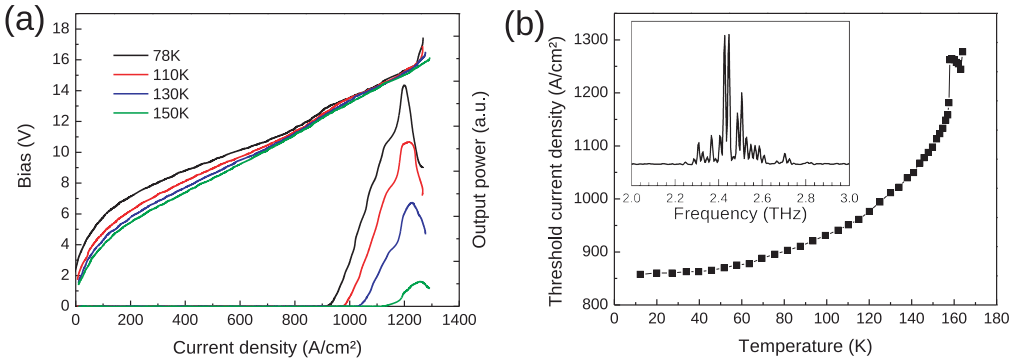

Fig. 2. (a) Light-current and voltage-current characteristics at different temperatures for sample L207. The devices were processed as laser ridges, 2 mm long and 200 μm wide. The threshold current density is 910 A/cm^2 at 78K (860 A/cm^2 at 10 K). The devices were operated with 300 ns pulses at a 20 kHz repetition rate; detection was achieved with a liquid-helium cooled silicon bolometer, and using f/1 collection optics. The peak output power of these metal-metal Fabry-Perot THz lasers is typically in the sub-mW range. (b) Laser threshold current density as a function of heat-sink temperature for a typical device. T_{max} is 165 K. Inset: Typical laser spectrum at T=10 K

3. Photonic crystal design, fabrication and spectral characterization

While this THz laser exhibits excellent temperature performance, its far-field emission pattern (data not shown) - as for any metal-metal THz QC laser - is extremely divergent [9, 14]. Here we employ the PC technology demonstrated in Ref. [11] to overcome this problem. The goal is to operate the device on a band-edge state of a PC resonator where low group-velocity states exist and lasing can occur. The optical mode is spatially delocalized over a large area, thus leading to a reduced angular spread of the output beam [11].

An image of a typical device is shown in Fig. 3(a): the photonic structure is defined in a technologically straightforward way by patterning of the top metallic contact alone. The possibility of doing this originates from the extremely high optical confinement achieved in metal-metal waveguides [15]. The PC design is based on a trigonal lattice, implemented as a triangular array of holes in the top device metallization only (Fig. 3(a)). The photonic-band structure of the infinite lattice has been calculated by solving the Helmoltz equation in a 3D single-unit cell of the triangular lattice, with Bloch periodic boundary conditions applied at the plane boundaries. The resulting band-structure (Fig. 3(b)) allows one to infer the correct PC dimensions in order to overlap spectrally the material gain with the regions of small group velocity, where candidate modes for lasing are expected to occur.

We have chosen to operate the devices at the Γ-point band-edge states located at $a/\lambda = 0.33$ in reduced energy (Fig. 3(b)), where a is the PC period and λ is the wavelength. These band-edge states are located above the light cone, and surface-emission should be obtained. Figure 4 (central panel) shows a magnified diagram of the photonic band-structure at the Γ point around the region of interest at $a/\lambda = 0.33$. Six different states are present, whose electric field distributions are shown in panels A-D. Note that band-edge states A and B are doubly

#106640 - $15.00 USD Received 21 Jan 2009; revised 3 Apr 2009; accepted 5 Apr 2009; published 22 May 2009

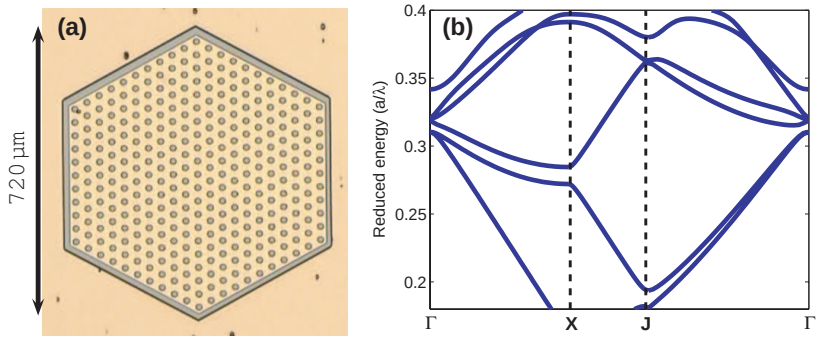

Fig. 3. (a) Optical microscopy image of a typical device. The PC pattern is written into the top metallic surface only. No semiconductor etch is used. (b) Photonic band structure for TM polarized light in the trigonal structure used for the experiments (see (a)), with an r/a ratio of 2/9 (0.222). The calculation has been performed in three dimensions, using Bloch-periodic conditions applied at the unit cell boundaries. The metal is approximated to be perfect, and the active region is modeled with a purely real effective index $n_{eff} = 3.6$.

degenerate. In the figure the degeneracy is lifted slightly owing to numerical inaccuracies in the simulations.

We have fabricated a series of devices with PC periods, a, ranging from $a = 34\ \mu m$ to $a = 38.9\ \mu m$. These values were chosen in order to overlap the material gain spectrum with the band-edge states at the Γ-point. The r/a ratio has been fixed at 0.22, where r is the PC hole radius. The devices comprise ten PC periods from the centre of the mesa (see Fig. 3(a)). Absorbing boundary conditions are implemented at the device boundaries following the procedure described in Ref. [11], where the crucial role of the boundaries is demonstrated. Typical laser spectra at T=78 K for several devices are shown in Fig. 5(a). The emission is collected from the device surface using an f/2 parabolic mirror. Two main modes (marked with dotted gray lines) are evident, which clearly tune with the PC period. Note that the spectra are acquired at the maximum output power, which might explain the presence of additional, weaker emission peaks in some of the spectra. In fact, at lower injection currents, close to J_{th}, the laser emission is always single mode. The origin of the additional, weaker emission peaks is unidentified at present; they might result from imperfections in the devices.

Figure 5(b) shows a typical L-V-I characteristic at liquid nitrogen temperatures (T=78 K) for a PC device. The peak output power reaches 4 mW (7 mW at 10 K) under pulsed operation, and the maximum operating temperature T_{max} is typically 136 K. The T_{max} for the PC devices is 30 K lower than for ridge devices. We do not yet have a definitive explanation for the reduced T_{max} of the PC devices compared with ridge lasers fabricated with the same epitaxial material; this might originate from the higher losses of the PC devices or from the non-uniform current injection resulting from the top metal geometry.

4. Mode identification based on the spectral characteristics

Figure 5(a) shows that the PC resonator mainly supports two lasing modes, whose frequencies tune with the photonic-lattice period. The distance between the modes is 13% of the central frequency, which is larger than the typical THz QC laser gain bandwidth. However, we have shown in Fig. 2(b) (inset) that the three-well QC structure used in this work gives a larger than usual bandwidth. This is the reason why three of the fabricated PC devices (corresponding to $a = 36.8\ \mu m$ to $a = 38.2\ \mu m$) can lase *simultaneously* on both resonator modes.

#106640 - $15.00 USD Received 21 Jan 2009; revised 3 Apr 2009; accepted 5 Apr 2009; published 22 May 2009

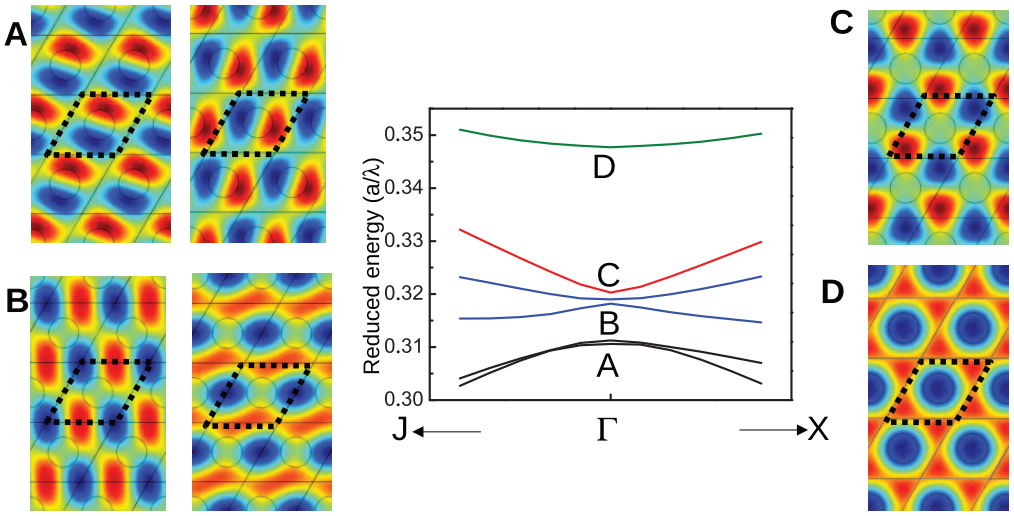

Fig. 4. Central Panel: Magnified view of the photonic band structure around the Γ point, with the reduced energy corresponding to the fabricated devices indicated. The electric field distributions (E_z) of the band-edge states located at the Γ point of the photonic band structure (labeled A, B, C and D) are also shown. The calculation has been performed for an infinite, periodic lattice with E_z, i.e. the electric field normal to the plane, shown as a color-scale. The area surrounded by the dotted black lines corresponds to the unit cell used in the calculation, and the values of the field at the center of the active region are shown. The circles correspond to the holes in the top metallization. The band-edge A (bipole) and B (quadrupole) are doubly degenerate. The band-edge C (hexapole) and D (monopole) are non-degenerate.

In order to identify which band-edge states A, B, C or D (Fig. 4) are lasing, it is instructive to plot the spectra in reduced units, as shown in Fig. 6. The black dashed lines represent the predicted position of band-edges C and D (in reduced frequency units) as a function of the PC period. The calculation is performed in 3D using a unit cell with Bloch periodic boundary conditions. The predicted and experimental tuning rates are in very good agreement, thus providing a first indication that the mode at $a/\lambda = 0.315$ is the hexapole mode (band-edge C) and the mode at $a/\lambda = 0.360$ is the monopole mode (band-edge D). This conclusion will be confirmed in the following sections by careful analysis of each device's far-field emission pattern and polarization. (Note: the agreement between predicted and experimental spectral positions of the modes is only fair, since the experimental splitting is approximately 35% larger. This can be explained by the simplifications employed in the numerical simulations, which were imposed by its 3D character. A perfect metal was used, the top n-doped layer below the metallic contacts was neglected, and the hole dimensions and shape were simplified).

The deviation of the band-edge D mode from the ideal behaviour $a/\lambda = constant$ can be explained intuitively. The laser active region thickness is fixed and does not change with the PC lattice spacing. As a consequence, the linear scaling typical of photonic crystals - which yields the "$a/\lambda = constant$" principle - is not valid in our case, and the effect on all modes is not identical. The modes whose electric field is mostly localized below the metallized regions, such as the hexapole mode (C-mode), will be almost unaffected, since the effective index of a metal-metal waveguide is largely insensitive to its thickness. On the other hand, the modes with a large concentration of energy below the non-metallised regions (such as the monopole mode, see Fig. 4) will be more sensitive because penetration into the air-cladding does depend

#106640 - $15.00 USD Received 21 Jan 2009; revised 3 Apr 2009; accepted 5 Apr 2009; published 22 May 2009

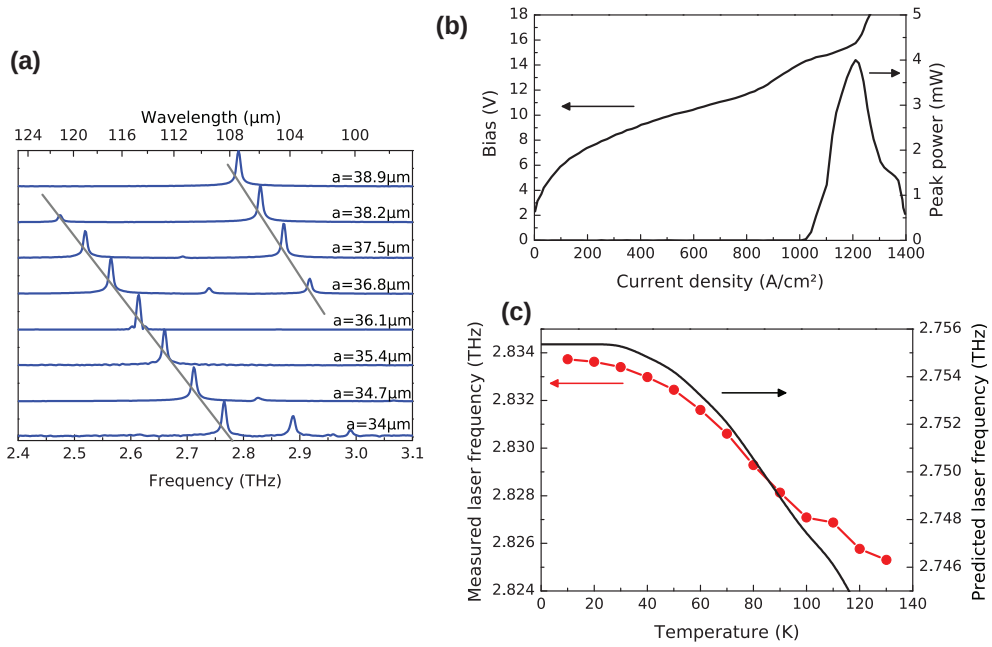

Fig. 5. (a) Laser spectra at T=78 K for different values of the PC period, *a*. In each case, injection currents were used that gave the highest laser output power. The spectra - which are offset for clarity - were acquired using an FTIR spectrometer, operating in rapid scan mode with a resolution of 0.125 cm^{-1} and a DTGS far-infared detector. The PC principally supports two modes. (b) L-I and V-I characteristics at a heat-sink temperature of 78 K of a PC device. The lattice period is 36.1 μm, and the T_{max} was 136 K. Other lasers with different PC periods all exhibit a T_{max} higher than 127 K, except for the device with period 38.9 μm, which lased up to 110 K. (c) Temperature dependence of the emission frequency of a PC laser with a period equal to 38.2 μm (red curve). A temperature tuning of 8 GHz was obtained between 10 K and 130 K. At low temperature, the non-linear temperature tuning can be explained using the static variation of the refractive index of the GaAs. The black line represents the numerically calculated emission frequency using the temperature dependence of the static refractive index of GaAs.

on the structure thickness. The clear deviation of mode D in Fig. 6 from the $a/\lambda = constant$ line therefore corroborates its identification as the monopole mode.

5. Wavelength tuning with operating temperature

Figure 5(c) shows the variation of the laser emission frequency of a PC device ($a = 38.2\ \mu m$) with heat sink temperature. The non-linear variation of the temperature tuning rate (mainly for temperatures below 40 K) has been already observed for first-order distributed feedback THz QC lasers [16]. It originates from the temperature dependence of the refractive index of GaAs. Unfortunately, to the best of our knowledge, complete data on the low temperature index of GaAs at THz frequencies is not available. However, the frequency dependence of the refractive index should be very low below a material's Restrahlen band, allowing the use of the static index [17] instead of the dynamic one. In Fig. 5(c), the black solid line represents the lasing frequency calculated with a 3D Bloch-periodic numerical simulation. The laser active region was modelled as a bulk GaAs slab, with its static refractive index depending on the heat-sink temperature. The global trend of the experimental data is in good agreement with the

#106640 - $15.00 USD Received 21 Jan 2009; revised 3 Apr 2009; accepted 5 Apr 2009; published 22 May 2009

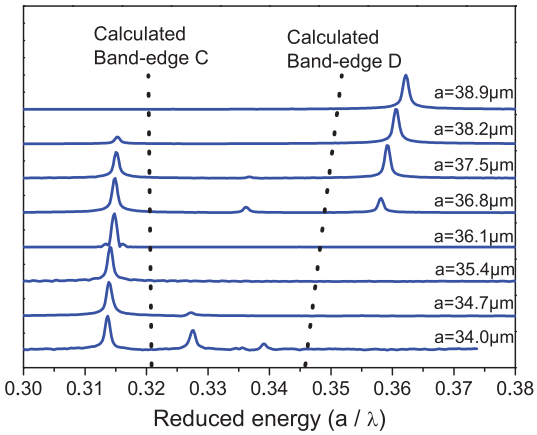

Fig. 6. Laser spectra at T=78 K for different values of the PC period (as in Fig. 5(a)), plotted in reduced frequency units (a/λ). The dotted lines correspond to the predicted spectral positions of the band-edge C (hexapole) and the band-edge D (monopole) modes. The spectra are offset for clarity.

simulations. The observed, tiny frequency difference between theory and experiment is possibly a result of the slight difference between the static and the actual GaAs refractive index.

6. Mode identification based on the far-field properties: numerical simulation details

The far-field emission patterns of the devices have been numerically simulated using the formalism developed in Refs. [18, 19]. The near-field of the different band-edge modes of the finite-size PC resonator was obtained using a 2D finite-difference time domain (FDTD) simulation [20], performed using a freely available software package (MEEP) [21] (Figs. 7a, 8a, 8e). The detailed 3D structure was replaced in an effective index approximation by an index n_{eff}=3.6 for the metalized regions, and by an index n_{eff}=2.8 for the holes. These values correspond to the real part of the effective index obtained by 1D simulations of the exact vertical structure. The value 3.6 corresponds to the index of the fundamental optical mode in a 10-μm-thick, metal-GaAs-metal structure. The value of 2.8 corresponds instead to an air-GaAs-metal structure of the same thickness. The simulated region is typically a square. Mur's absorbing boundary conditions were implemented by surrounding the PC hexagonal structure with a 'layer' of index n=3.6 terminated by a perfectly matched layer (PML). This procedure guarantees that the energy emerging from the PC edge will travel without reflection into the surrounding layer, and will impinge the PMLs [22].

In order to calculate the far-field emission pattern, we need the transverse electric and magnetic field components in the device near-field. These values are not provided by a 2D simulation. We therefore employed the following approximation: since the top metallization is much thicker than the metal skin depth at the laser wavelength, it is reasonable to assume that the energy can flow out from the holes only. We have therefore set the transverse magnetic field to zero in the metalized regions, and only the field inside the holes is employed to perform the near-to-far-field transformation using the standard Fourier-transform approach [18, 19]. The validity of this procedure has been tested by performing the full 3D simulation on a few band edge modes; the far-field patterns obtained within the 3D approach show no significant difference from the 2D simulations described above, which have the advantage of requiring a much lower computational power.

Two kinds of simulations have therefore been used throughout this work. The infinite, pe-

#106640 - $15.00 USD Received 21 Jan 2009; revised 3 Apr 2009; accepted 5 Apr 2009; published 22 May 2009

riodic system has been modelled with 3D finite-elements simulations using Bloch-periodic boundary conditions (see Fig. 1). However, the finite system (the PC cavity) has been analysed using 2D FDTD simulations. The two strategies are complementary: the objective of the 3D simulations is the determination of the photonic band structure, and of the frequencies for the relevant band-edge states at the Γ-point of the photonic dispersion. The 2D simulations allow the calculation of the far-field emission patterns. It should be noted that the 3D simulations were simplified in order to reduce the computational power required: a perfect metal approximation was used, and the thin top and bottom contact layers neglected. However, the optical feedback in this kind of PC structures is mainly given by the mismatch between the guided modes existing in the metallised and non-metallised regions, and not by a variation of the refractive index. The 3D character of the band-structure simulations correctly accounts for this effect. In contrast, the 2D simulations do not provide an accurate prediction of the lasing frequencies of the *finite* structure. They rely on an effective index approximation and do not capture the true nature of optical feedback. However, they do reproduce correctly the symmetry of the modes, and are therefore ideally suited to simulate the device far-field emission. The far-field patterns in fact depend on the geometry and on the symmetry of the mode over the whole structure, and not strongly on the lasing frequency.

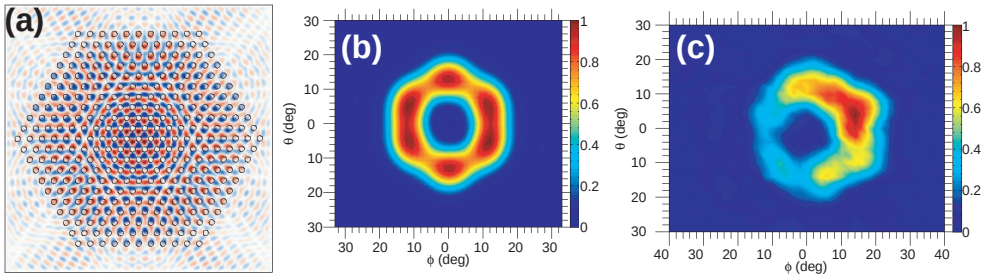

Fig. 7. (a) Electric field distribution (E_z component) - obtained with a 2D FDTD simulation - for the band-edge hexapole mode labeled C. The size of the simulation field is 800 x 800 μm^2, and it encompasses the whole device surface. PML layers are placed at the boundaries of the simulation field. (b) Calculated far-field profile for the hexapole mode represented in (a). The far-field has been obtained using the transverse magnetic near-field in the metal holes only. The field outside the holes, i.e above the metal surface, was assumed to be zero. (c) Experimental far-field pattern of the mode at $a/\lambda = 0.315$. The measurement has been performed at 78 K by scanning a Golay cell detector at a constant distance from the laser.

7. Mode identification through the far-field properties: experimental measurements and analysis

The far-field patterns were collected by scanning a room-temperature Golay cell detector with a 2 mm aperture on a 6-cm-radius sphere centered on the device. The $\phi = 0$, $\theta = 0$ angle corresponds to the direction orthogonal to the device surface. Figure 7(a) shows the theoretical near-field for a PC device operating on the hexapole mode, labelled C in Fig. 4. The E_z component of the field is shown. The corresponding calculated far-field, obtained by the procedure described above, is shown in Fig. 7(b). Figure 7(c) shows the experimental far-field pattern of a PC device ($a = 36.1\ \mu m$). The agreement with theory is good and we assign the emission to the hexapole mode. The mode symmetry and the angular values are correctly reproduced, although the experimental far-field exhibits an asymmetric intensity. The emission at $a/\lambda = 0.31$

#106640 - $15.00 USD Received 21 Jan 2009; revised 3 Apr 2009; accepted 5 Apr 2009; published 22 May 2009

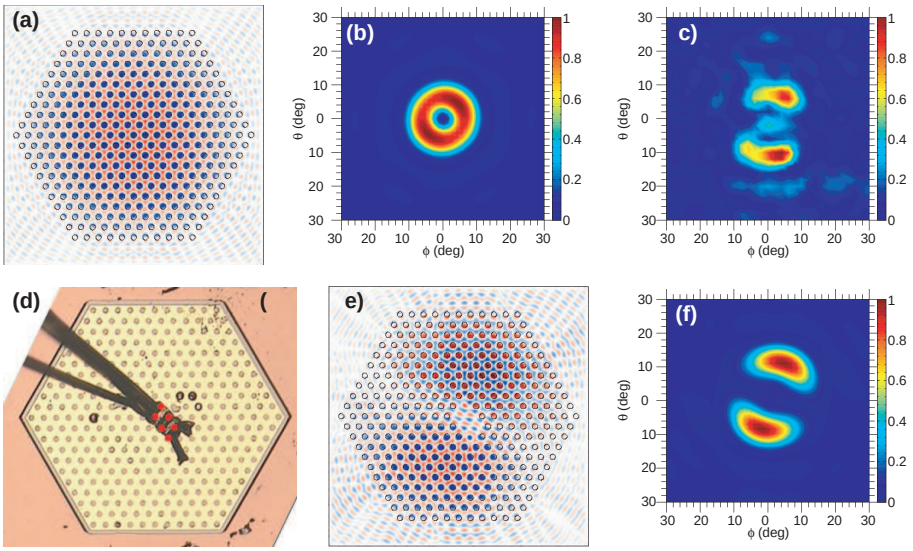

Fig. 8. (a) Electric field distribution (E_z component) - obtained with a 2D FDTD simulation - for the band-edge monopole mode labeled D. The highest Q factor mode is shown. (b) Calculated far-field pattern obtained from the near-field profile in (a). (c) Experimental far-field pattern of the mode at $a/\lambda = 0.36$. (d) Optical microscopy image of the measured device. The red circles mark the position of the holes masked by bonding. (e) E_z - obtained with a 2D FDTD simulation - for the band-edge monopole mode labeled D when the presence of the bonding wire - as shown in (d) - is taken into account. Unlike (a), the envelope function now exhibits a nodal line. (f) Calculated far-field pattern obtained from the near-field in (e). The experimental far-field profile (c) is in excellent agreement with theory when the effect of the bonding wires are taken into account.

is therefore identified.

For the emission at $a/\lambda = 0.36$, which we have assigned to the monopole mode, the theoretical near-field is shown in Fig. 8(a) and the corresponding calculated far-field in Fig. 8(b). However, the experimental far-field pattern of a PC device operating at $a/\lambda = 0.36$ is quite different (Fig. 8(c)). To understand this result, it is important to take into account the position of the wire bonding which covers a few holes in the PC pattern, as shown in Fig. 8(d). The presence of the bond wire can be implemented in the simulations by assuming that it fills some holes with metal: a hole covered by the bond wire simply exhibits an effective index of 3.6 instead of 2.8. Figure 8(e) shows the electric field normal to the photonic crystal plane (E_z) for the same device as Fig. 8(a), but in the presence of a central bonding wire. The represented field corresponds to the mode with the highest Q-factor. The corresponding theoretical far-field emission pattern is shown in Fig. 8(f); it is in excellent agreement with the experiment, and confirms that the mode emitting at $a/\lambda = 0.36$ originates from band-edge D.

The device electromagnetic near-field is composed of a spatially rapidly oscillating part - which stems from the symmetry of the band-edge state - and of a slowly varying component which can be seen as an envelope function. The latter is the component that is affected by the presence of the bonding. In particular, for the device operating on band-edge D, in the absence of bonding (Fig. 8(a)) the envelope function shows no nodal points, whilst when a central bonding is applied, a nodal line appears (Fig. 8(e)). This phenomenon explains the

#106640 - $15.00 USD Received 21 Jan 2009; revised 3 Apr 2009; accepted 5 Apr 2009; published 22 May 2009

experimental results for the monopole mode (Fig. 8), but - remarkably - it is not relevant for a device operating on the hexapole mode (Fig. 7).

It should be noted that the possibility of lasing on a monopole mode is a peculiarity of this system, where no holes are etched in the semiconductor material, but only in the top metallization. Optical gain is therefore preserved in the regions where no top metallization is present.

8. Polarization measurements

The polarization in the far-field was measured by scanning a helium-cooled silicon bolometer on a plane parallel to the sample surface, at a distance of 12 cm, with a polarizer placed just before the bolometer input window. For each point, four measurements were acquired: the polarization angle of the maximum signal and the corresponding value (I_{max}); and, the polarization angle of the minimum signal and the corresponding value (I_{min}). In Figs. 9(a) and 9(c) (experimental measurements) the directions of the arrows correspond to the electric field directions, whilst the lengths represent the polarization ratio, as follows:

$$Arrow-Length = p = \frac{I_{max}(\theta) - I_{min}(\theta)}{I_{max}(\theta) + I_{min}(\theta)} \tag{1}$$

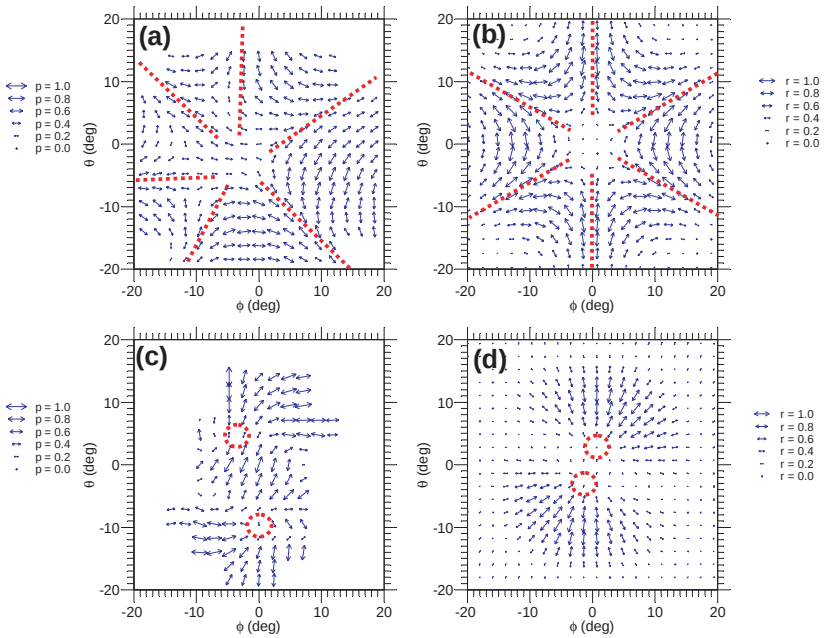

Fig. 9. Polarization in the far-field: a comparison between theory and experiment. The arrows represent the electric field direction. (a) and (c) show experimental data for devices operating on the hexapole (C) and monopole (D) modes, respectively. One point in two has been measured, the other points are obtained through interpolation. The directions of the arrow correspond to the maxima of the electric field polarizations. The length of the arrows represent the ratio $p = (I_{max} - I_{min})/(I_{max} + I_{min})$. The greater the length of the arrow, the closer the polarization is to linear. The dotted lines are guides to the eye. (b) and (d) show simulations of the far-field polarization for the hexapole and monopole modes, respectively, taking into account the bonding. The length of the arrows represents in this plot the calculated farfield intensity (r values on the right scale) normalized to one.

#106640 - $15.00 USD Received 21 Jan 2009; revised 3 Apr 2009; accepted 5 Apr 2009; published 22 May 2009

(Note: one data point in two has been measured for each axis. The other data-points are obtained through a linear interpolation). The longest arrows indicate a mostly linear polarization. Figures 9(b) and (d) show the theoretical polarization in the far-field, calculated using a similar procedure. For the hexapole mode (band-edge mode C), a six-fold symmetry can be clearly identified. The radial directions of polarization are highlighted with red dotted lines and are present in both the experiment and the numerical simulations. For the monopole mode (band-edge mode D), the comparison is more difficult, but two attraction points (circled by red dashed lines) can be clearly identified in both the experimental data and the simulations. The qualitative agreement between the theory and the experimental polarization measurements further strengthens the case for identifying lasing as occurring on the hexapole and monopole modes.

9. Conclusions

We have shown that it is possible to engineer the far-field emission pattern of THz PC QC lasers predictably. A theoretical framework has been developed and applied to high-performance THz heterostructure lasers, which have metal-metal waveguide geometries and operate at $\approx$ 2.7 THz. The PC QC lasers operate up to a temperature of 136 K. The results also show that the presence of the bonding wires has an important effect on the far-field emission and must be taken into account. However, since the effect of bonding wires is predictable, this can also be exploited as a tool to engineer the emission pattern.

Future work will focus on the development of PC THz semiconductor lasers emitting from the surface into a single, narrow lobe, and on the reduction of the injected power. The combination of good performance, controllable emission properties and relatively simple technological implementation suggests that this device architecture - based on metallic PCs - could prove invaluable for commercial exploitation.

Acknowledgments

We thank S. Kumar, F. Julien, and C. Sirtori for useful discussions. The device fabrication has been performed at the CTU-IEF-Minerve which was partially funded by the ”Conseil Général de l’Essonne”. This work was conducted as part of a EURYI scheme award (see www.esf.org/euryi). We also acknowledge support from the UK’s Engineering and Physical Sciences Research Council and Her Majesty’s Government Communications Centre (SPK).

#106640 - $15.00 USD Received 21 Jan 2009; revised 3 Apr 2009; accepted 5 Apr 2009; published 22 May 2009